Available online at www.sciencedirect.com
ScienceDirect
Earth and Planetary Science Letters 260 (2007) 227–241
EPSL
www.elsevier.com/locate/epsl

The partitioning of water between olivine, orthopyroxene and melt synthesised in the system albite–forsterite–H_2O

Kevin J. Grant *, Simon C. Kohn, Richard A. Brooker [1]

Department of Earth Sciences, University of Bristol, Wills Memorial Building, Queens Road, Bristol, BS8 1RJ, UK

Received 19 December 2006; received in revised form 16 May 2007; accepted 19 May 2007
Available online 26 May 2007
Editor: T. Spohn

Abstract

Coexisting forsterite, enstatite and silicate glass were synthesised from a water-bearing basalt analogue in programmed cooling experiments at 1.0, 1.5, 2.0 and 2.5 GPa. Hydrous species in each phase were characterised and quantified using infrared absorbance spectroscopy. Al^{3+}-related hydroxyl defects, with vibrational energies between 3400–3200 cm^{-1}, dominate the hydroxyl budget of synthetic forsterite. The vibrational characteristics of these defects indicate that similar absorptions in Fe-bearing systems result from Fe^{3+}-related OH species. This interpretation resolves a previously recognised, but unexplained, relationship between oxygen fugacity and hydroxyl speciation in experimentally annealed olivines, and suggests that the intensities of bands at 3400–3300 cm^{-1} could form the basis of an oxybarometer.

OH defect speciation in enstatite is similar to that in aluminous crystals synthesised at high water fugacity and many natural orthopyroxenes. Hydroxyl speciation in orthopyroxene is not, therefore, controlled by water activity. Total water contents of synthetic enstatites from any single experiment vary enormously. This heterogeneity is attributed to variable contributions from a non-intrinsic broad-band hydrous component. Intrinsic hydroxyl concentrations dissolved in enstatite are identical in all crystals from an experiment.

The partitioning of water between forsterite, enstatite and coexisting silicate melt is independent of pressure, temperature and total water content over the range of conditions studied, as long as the influence of these parameters on phase compositions is taken into account. $D_{H_2O}^{Fo/melt}=0.0001–0.0003$ ($n=4$) and is insensitive to pressure or olivine aluminium contents. $D_{H_2O}^{En/melt}$ is strongly controlled by Al_2O_3 concentration and ranges from 0.003–0.016 ($n=6$). Two samples contain both forsterite and enstatite and yield $D_{H_2O}^{En/Fo}=25\pm1$.

Keywords: water; partition coefficient; upper mantle

1. Introduction

Water exerts a fundamental control upon the physical properties and melting characteristics of rocks (Karato, 1990; Wood, 1995; Hirth and Kohlstedt, 1996; Regenauer-Lieb and Kohl, 2003; Hirschmann et al., 2005; Wang et al., 2006; Yoshino et al., 2006). Recognising the effect of different physicochemical

* Corresponding author. Present address: ARC Key Centre for the Geochemistry and Metallogeny of the Continents (GEMOC), Department of Earth and Planetary Sciences, Macquarie University, NSW, Australia. Tel.: + 61 29850 8258; fax: +61 29850 8943.
E-mail addresses: Kgrant@els.mq.edu.au (K.J. Grant), Simon.Kohn@bristol.ac.uk (S.C. Kohn), Richard.brooker@ucl.ac.uk (R.A. Brooker).
[1] Present address: Department of Earth Sciences, University College London, Gower Street, London. WC1E 6BT, UK.

0012-821X/$ - see front matter © 2007 Elsevier B.V. All rights reserved.
doi:10.1016/j.epsl.2007.05.032

parameters on the partitioning of water between silicate phases comprising the upper mantle is critical before we can satisfactorily explain many deep-earth processes, understand volatile cycling in the Earth and constrain models of planetary evolution.

Hydrous defects dissolved in silicate phases comprising peridotite xenoliths yield information about hydroxyl speciation at ambient conditions (Grant et al., 2007). However, it is becoming increasingly evident that correlating hydroxyl in mantle silicates with that at depth in the Earth is extremely complicated (Ingrin and Skogby, 2000; Ingrin and Blanchard, 2006). Carefully controlled experiments, conducted on relatively simple chemical systems, are the key to better understanding how hydrous species partition between phases in the upper mantle of the Earth. Despite this, however, the literature on the subject remains sparse. Previously we described hydroxyl partitioning between enstatite, forsterite and melt in the system $MgO–SiO_2–H_2O$ and showed that, at 2.0 GPa and 1350 °C, near end member enstatite contained on average three times as much hydroxyl as coexisting forsterite (Grant et al., 2006). These results highlighted the physical controls influencing hydroxyl solubility in olivine and orthopyroxene and illustrated the important factors controlling the distribution of hydrous species between these phases. Natural systems are, however, significantly more complex and so further work was needed to develop our understanding. Here we describe the results of additional high-pressure and temperature experiments. In these, coexisting olivine, orthopyroxene and a quenchable silicate melt were synthesised from a chemically more complex starting composition than our previous study (Grant et al., 2006). The advantage of conducting these experiments in the chosen chemical system is that the phase assemblage remains similar throughout crystallisation of the constituent phases and it can be loosely interpreted to represent a simplified basalt analogue. Thus, our new data provides important information about how hydrous species partition between these key phases in the mantle and crust.

2. Experimental procedures

2.1. Starting materials

Experiments were conducted using a bulk composition in the iron-free, albite–forsterite–H_2O system (hereafter referred to as Alb–Fo–H_2O). The appropriate proportions of reagent grade SiO_2, Al_2O_3, and Na_2CO_3 were mixed together, melted in a platinum crucible at 1300 °C for 12 h and quenched in water to form a glass. This was then crushed to a fine powder in an agate mortar and the necessary quantity of high-purity brucite ($MgOH_2$) added. The resulting starting mixture (ALBH), which was used as starting materials for experiments ALB5, ALB6, ALB7, ALB9 and ALB10, contains approximately 7 wt.% H_2O. A proportion of starting material ALBH was then dehydrated overnight in a furnace to generate anhydrous mixture ALBD. The results of electron microprobe analyses of a fragment of ALBD, which was re-melted at 1400 °C for 1 h and then quenched to form a glass, are presented on Table 1. Starting material for ALB13 was prepared by mixing ALBH and ALBD in a ratio of 1:1. ALB14 contained one part by weight ALBH for two parts ALBD.

2.2. High-pressure experiments

High-pressure and temperature experiments were conducted in an end-loaded 3/4 in. diameter, piston cylinder apparatus at the University of Bristol. Details of the pressure calibration and thermocouple arrangement are described elsewhere (McDade et al., 2002).

Experiments were conducted in capsules formed from 6.0 mm OD (5.6 mm ID) platinum tubing. Starting powders were tightly packed into the capsules. These were then welded shut and placed into 3/4 in. diameter talc–pyrex piston cylinder assemblies. A tapered graphite heater in the cell assembly ensured that the temperature of the experiment was within 10–20 °C of that measured by the thermocouple, (Y. Morizet, personal communication).

Each experiment was initiated by increasing sample pressure to 0.5 GPa and heating to 500 °C. This softened the pyrex sleeve glass sleeve. Sample pressure was then increased to the required value and the sample heated at 9000 °C/h to the temperature required to start the experiment.

2.3. Crystal growth

Preliminary experiments were conducted to determine the liquidus temperature of ALBH at 1.5 GPa. To

Table 1
Major element chemistry of starting material ALBD

	SiO_2	Al_2O_3	MgO	FeO	CaO	Na_2O	K_2O	Total [a]
Measured [b]	63.28	14.14	15.59	0.00	0.016	5.92	0.02	100
Calculated [c]	60.93	13.61	17.19	0.00	0.00	8.27	0.00	100

[a] Oxide totals normalised to 100%.
[b] Determined by electron microprobe on a fragment of starting mixture ALBH that was melted at 1400 °C for 1 h and then quenched to form a glass (*i.e.* ALBD).
[c] Calculated bulk chemical composition.

grow the large, high quality crystals necessary for FTIR analyses, synthesis experiments involved slowly cooling from an initial temperature above the liquidus (T^i). Samples were held at T^i for between 5 min and an hour. ALB5, ALB7, ALB13 and ALB14 were then cooled at 80 °C/h from T^i to T^m. All experiments were then cooled slowly from T^i or T^m to the required final temperature (T^e) at between 1 and 3 °C/h (Table 2).

Using this method, crystals in excess of 1 mm in length were synthesised. The main disadvantage of this technique, however, is that the precise crystallisation temperature of any given point in a crystal is not known exactly. This is more problematical for electron microprobe analyses than for FTIR because the analytical spot of the later is much larger and the corresponding spectrum represents an average across the thickness of the double-polished slice (see below). Growth rate may influence the hydroxyl contents of a crystal (Lemaire et al., 2004) and so experiments were conducted using different cooling paths (Table 2). Experiments were also conducted using identical experimental procedures but with different initial water contents (starting mixtures of ALB6, ALB13 and ALB14 contained approximately 7, 5 and 2 wt.% H_2O respectively).

2.4. Investigation of run products and sample preparation

The Pt capsule was carefully pierced after each experiment. Free water was not observed coming from any of the capsules. The capsule was then fully opened and the contents subject to preliminary investigation under a binocular microscope. Crystals and glass fragments were separated from the bulk sample, placed onto a glass microscope slide, oriented according the crystallographic axes and set in a cold cured acrylic resin. Wherever possible, crystals and a section of the adjacent glass were analysed together. Glass fragments distant to crystalline phases were also prepared for analysis. After the resin had hardened, each sample was prised from the glass slide using a scalpel, ground on both sides to expose the crystal and finely polished using diamond-coated lapping film. Each sample was then re-inspected under an optical microscope to identify regions free of inclusions and fractures. We attempted to prepare and analyse at least 10 different crystals of each phase from every capsule.

2.5. Infrared spectroscopy

Infrared spectra were collected using a SpectraTech infrared microscope coupled to a Nicolet Nexus Fourier transform infrared spectrometer. The entire infrared microscope unit was sealed in an airtight box and continually purged with dry air to reduce the H_2O background. Wafers were placed on the sample stage of the microscope at least 12 h prior to analysis. This procedure significantly decreased spectral contamination by atmospheric water and proved essential in increasing the signal to noise ratio for quantitative measurements.

Polarised analyses of olivine and orthopyroxene were conducted using a globar™ source, KBr beamsplitter and a liquid nitrogen cooled MCT detector. Spectra were measured between 5500 and 650 cm^{-1} and 256 or 516 scans were collected at a resolution of 4 or 8 cm^{-1}. Polarisation of the beam was achieved using a ZnSe polariser located in the infrared microscope unit.

Unpolarised absorbance spectra of synthetic glasses were collected on specially thinned wafers using the same experimental setup as described above for the analysis of the silicate phases, and using near infrared measurements. Near infrared spectra were collected between 6000 and 2000 cm^{-1} using a white light source, KBr beamsplitter

Table 2
Summary of experimental conditions and run products identified

	P (GPa)	T^i (°C)	T^m (°C)[a]	Rate[b] (°C/h)	T^e (°C)	Duration (h)	Initial H_2O (wt.%)	Phases present after experiment	Phases analysed by IR
ALB5	1.5	1450	1320	1	1295	26	7	En, Fo, Sp, melt	En, Fo, melt
ALB6	1.5	1450	–	2	1320	65	7	En, Fo, melt	En, Fo, melt
ALB7	2.0	1460	1330	1	1305	26	7	En, melt	En, melt
ALB8	2.0	1480	–	2	1339	75	7	En, Fo, melt	Fo, melt
ALB9	2.5	1480	–	3	1330	50	7	En, melt	En, melt
ALB10	1.0	1450	–	3	1330	45	7	Fo, Sp, melt	Fo, melt
ALB13	1.5	1530	1400	2	1351	25	5	En, melt	En, melt
ALB14	1.5	1550	1450	1	1400	50	2	En, melt	En, melt

All samples were initially heated to T^i — the initial temperature at 9000 °C/h and remained at this for between 5 min and several hours.
[a] ALB5, ALB7, ALB13 and ALB14 were cooled from T^i to T^m at 80°C/h.
[b] Rate of cooling from T^m to T^e, the temperature at end of experiment (see text).

and a liquid nitrogen cooled MCT detector. Each glass sample was analysed in 3 to 10 different spots.

The thickness of each double-polished wafer was measured using a Mitutoyo digital indicator. Wafers of olivine, orthopyroxene and melt generally measured 25–150 μm, 150–350 μm and 15–450 μm in thickness, respectively. All raw spectra were normalised to a 1 cm pathlength.

Polarised spectra were collected on crystal wafers, which had been oriented according to crystallographic axes under an optical microscope. Crystallographic orientation was confirmed using the overtone and combination absorptions between 2400 and 1200 cm^{-1} in a manner similar to that described elsewhere (Jamtveit et al., 2001; Lemaire et al., 2004). Crystal alignment using this combined approach is estimated to be better than ±10°, an adequate level of precision for accurately measuring OH band intensities on the resulting spectrum (Libowitzky and Rossman, 1996).

2.6. SEM and microprobe

After infrared analysis, samples were mounted in EpoFix epoxy resin, prepared as polished blocks and imaged using a Hitachi S3500N scanning electron microscope. Electron microprobe analyses were then conducted using a Cameca SX100 electron microprobe and a Jeol 8600 superprobe at the University of Bristol. Hydrous glasses were analysed using a defocused beam, 10 nA beam current and a 15 kV accelerating potential. Mineral compositions were determined using a 20 nA beam current and a 15 kV accelerating potential. The same operating conditions were employed on each electron microprobe and repeat analyses conducted on both gave identical phase compositions.

2.7. LA-ICPMS

Aluminium contents of the forsterite crystals were measured *in situ* using LA-ICP-MS microprobe at Macquarie University. Analyses were conducted using a Merchantec 266 nm Nd:YAG laser in combination with an Argilent 7500 sc Octopole Reaction System ICP-MS. The system was operated in Normal mode without a Pt shield. The laser operated at 5 Hz and 0.8 mJ. Samples were analysed using a 60 μm analytical spot size. Each analysis lasted for a total of 200 s. The gas background was measured for approximately 100 s and the sample signal

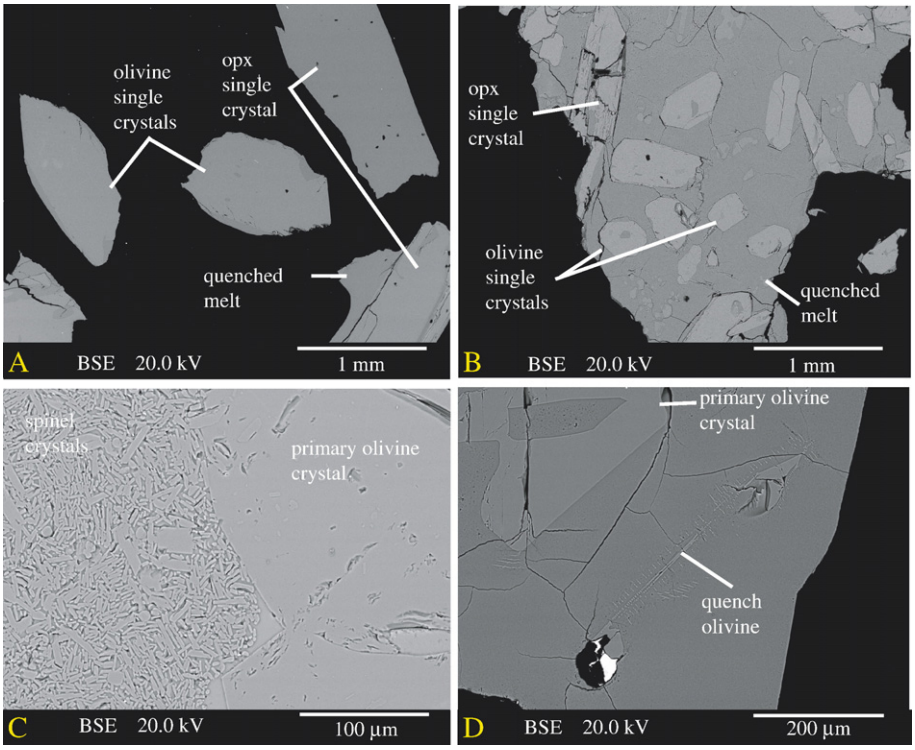

Fig. 1. SEM images of selected crystal morphologies recovered from synthesis experiments described in this study: A) large olivine and orthopyroxene crystals from ALB6. Crystals shown are embedded in resin; B) run product from ALB5; C) olivine and spinel from ALB10; D) primary and quench olivine from ALB5.

acquired for the remainder. Ablation was carried out using He gas mixed with Ar. Four forsterite crystals were analysed from each sample. Each analysis was normalised to SiO_2 contents as pre-determined by electron microprobe. Time-resolved signals were integrated and processed using GLITTER software. All elements were calibrated against the NIST610 trace element glass standard using published reference values (Norman et al., 1996). Independent checks were also made after each analysis using a BCR2G standard. Standard deviations (reported in brackets on Table 2) reflect variability in the aluminium concentration generated by the repeat analyses.

3. Results

3.1. Run products and sample petrography

Experiments were conducted at 1.0, 1.5, 2.0 and 2.5 GPa and cooled to final temperatures (T^e) of between 1295 and 1400 °C. Different proportions of enstatite, forsterite, spinel and glass were generated in each experiment (Table 2). Large, well-formed euhedral crystals are interpreted as the result of primary growth from the melt (Fig. 1A–D). These were easily separated from the bulk sample, oriented according to the crystallographic

Table 3
Average chemical compositions of phases synthesised in this study

	ALB5	ALB6	ALB7	ALB8	ALB9	ALB10	ALB13	ALB14
Melt								
Prop [a]	79	73	80	85	80	80	80	80
SiO_2	60.29 [33]	60.06 [32]	55.17 [25]	59.68 [35]	50.65 [98]	56.22 [68]	62.45 [23]	58.96 [39]
Al_2O_3	16.83 [146]	17.73 [36]	17.53 [12]	15.29 [13]	20.87 [91]	17.81 [16]	18.28 [8]	18.96 [25]
MgO	2.78 [38]	2.92[36]	9.13 [22]	8.38 [3]	11.34 [219]	9.96 [55]	9.68 [32]	8.46 [86]
CaO	0.13 [4]	0.12 [3]	0.21 [3]	0.03 [2]	0.42 [4]	0.41 [3]	0.02 [1]	0.07 [4]
Na_2O	10.25 [25]	10.81 [38]	9.07 [16]	9.65 [18]	5.76 [253]	8.48 [74]	5.55 [14]	11.36 [86]
K_2O	0.37 [15]	0.51 [12]	0.27 [5]	0.21 [5]	0.24 [13]	0.11 [1]	b.d.]	0.02 [2]
Total	92.17 [71]	92.19 [8]	91.44 [44]	93.27 [46]	89.55 [106]	93.55 [39]	96.14 [32]	96.84 [117]
Enstatite								
Prop [a]	6	14	20	2	20		20	20
SiO_2	59.56 [12]	59.42 [30]	59.60 [58]	58.28 [118]	56.25 [112]		59.05 [32]	58.38 [35]
Al_2O_3	0.84 [15]	1.00 [25]	1.06 [25]	2.16 [184]	6.39 [170]		1.47 [28]	2.46 [52]
MgO	39.11 [13]	38.97 [23]	40.07 [57]	38.63 [81]	36.66 [76]		40.70 [22]	38.00 [35]
CaO	0.01 [1]	0.01 [1]	0.01 [1]	0.02 [1]	0.03 [2]		0.02 [2]	0.01 [2]
Na_2O	0.05 [1]	0.06 [1]	0.05 [3]	0.05 [1]	0.15 [2]		0.13 [2]	0.12 [1]
K_2O	b.d.	b.d.	0.01 [1]	b.d.	0.01 [1]		0.01 [1]	0.00 [1]
Total	99.59 [14]	99.48 [30]	100.83 [51]	99.15 [27]	99.51 [58]		101.07 [28]	98.99 [27]
Olivine								
Prop [a]	12	13		13		13		
SiO_2	42.87 [23]	42.84 [33]		42.71 [26]		42.71 [23]		
Al_2O_3	0.03 [1]	0.03 [1]		0.04 [1]		0.04 [2]		
MgO	56.46 [36]	56.38[35]		56.22 [25]		56.29 [24]		
CaO	0.01 [1]	0.01 [1]		0.02 [5]		0.01 [1]		
Na_2O	0.01 [1]	0.01 [1]		0.01 [1]		0.01 [1]		
K_2O	0.01 [1]	0.01 [1]		0.01 [1]		0.01 [2]		
Total	99.91 [76]	99.42 [57]		99.09 [41]		99.22 [45]		
Al (ppm) [b]	228[109]	131[2]		177[70]		265[5]		
Spinel								
Prop [a]	3					5		
SiO_2	0.08 [2]					0.09 [7]		
Al_2O_3	72.22 [32]					72.61 [92]		
MgO	26.72 [26]					26.69 [85]		
CaO	0.01 [1]					0.01 [1]		
Na_2O	b.d.					0.02 [2]		
K_2O	b.d.					0.00 [1]		
Total	99.05 [20]					99.44 [26]		

[a] Phase proportions estimated by mass balance.
[b] Al contents were determined by LA-ICPMS.

axes and prepared as double-polished wafers (Fig. 1A). Melt inclusions were common in primary crystals (Fig. 1D), but these were easily avoided during analysis. Aggregates of enstatite and forsterite quench crystals were also present in several samples (Fig. 1D).

Because melt water contents were quite high, they quenched to form an opalescent white glass. Melt from ALB13 and ALB14, which contained 5 and 2 wt.% water in the starting mixture respectively, quenched to a form a transparent, clear glass. Alumina-rich spinel was found in ALB5 and ALB10 (Fig. 1C). Phase proportions were estimated by mass balance (Table 3), however, compositions determined using the electron microprobe do not always yield values that comprehensively agree with the starting composition and so the presence of undetected silica-rich phases or chemical zonation must, in several cases, be considered.

3.2. Mineral chemistry

The major element compositions of synthetic forsterite from each experiment are essentially identical (Table 3). Aluminium contents range from 100 to 250 ppm. There is no simple relationship between the amount of aluminium in forsterite and experimental *P* or *T*. Enstatite crystals from different experiments are compositionally distinct. Al_2O_3 and NaO contents vary from sample to sample but range from 1.0–6.4 and 0.05–0.15 wt.%, respectively. Occasionally, enstatite crystals from ALB6 and ALB9 were compositionally zoned but homogeneous crystals were also found in both experiments. Where present, chemical zoning in enstatite is manifested as Al_2O_3 depletion from core to rim. The amount of SiO_2 and MgO in glasses from each experiment varied according to the run but measured between 50–60 wt.% and 3–10 wt.% respectively. Throughout the experimental suite, glass Al_2O_3 contents ranged from 17 and 19 wt.% and Na_2O from 8 and 11 wt.%. Most glasses were chemically homogeneous, although the amount of Na_2O, SiO_2 and MgO in glasses from ALB9 varied slightly as a function of distance from the capsule wall (Table 3).

3.3. Hydroxyl in forsterite

Hydroxyl defect species dissolved in forsterite from ALB5, ALB6 and ALB8 are essentially identical (Fig. 2). Spectra measured where E||*a* and E||*b* are dominated by a strong absorption centred at 3346 cm^{-1} and two weaker peaks at 3381 and 3322 cm^{-1}. These

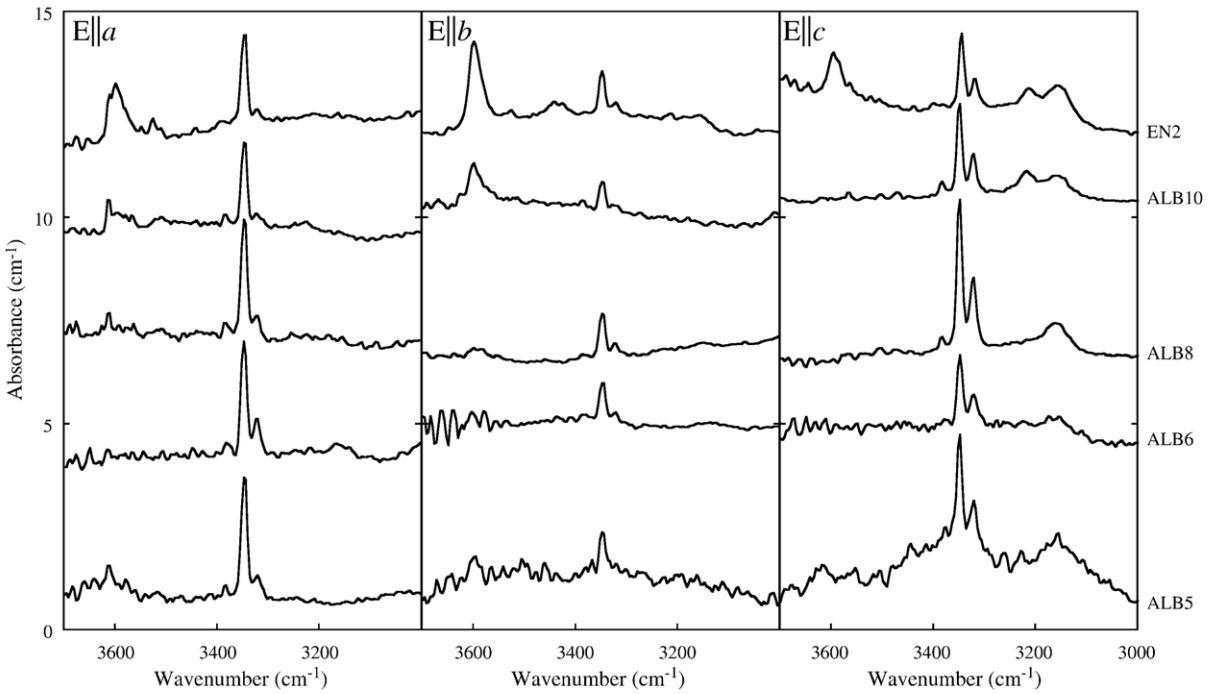

Fig. 2. Polarised infrared absorbance spectra of the OH stretching region in forsterite from samples ALB5, ALB6, ALB8 and ALB10 (this study) and EN2 (Grant et al., 2006). Spectra comprising the figure are single spectra (ALB5 E||*a* and E||*b* only) and the average of up to 6 separate spectra collected where the incident beam was aligned parallel to the *a*, *b* and *c* crystallographic axes. Spectra in all of the figures have been normalised to a 1 cm pathlength and may have been offset vertically to allow comparison between samples.

absorptions are also evident where E||*c*, as is an additional, broader, peak centred at 3160 cm^{-1}. The same hydroxyl defects are found in forsterite from ALB10 but crystals from this sample also contain absorptions at 3612, 3596 and 3566 cm^{-1}. The magnitudes of these later absorptions are, however, extremely weak when compared to those between 3400 and 3200 cm^{-1}. Forsterite from ALB10 also contains a double OH absorption at 3222 and 3160 cm^{-1}.

A background was subtracted from each raw polarised spectrum and individual OH peaks resolved using PeakFit software (Jandel Scientific). The integrated OH absorbance of each peak was converted to hydroxyl content using a wavenumber-dependant absorption coefficient for a peak of that energy (Paterson, 1982; Libowitzky and Rossman, 1997) (Table 4). Total hydroxyl contents were quantified for each sample by summing the contribution of all OH absorptions on averaged spectra collected parallel to each crystallographic direction and by resolving individual OH modes on the background-subtracted total spectrum ($A^{tot}=A^{E||a}+A^{E||b}+A^{E||c}$). Both methods yield identical OH concentrations. Hydroxyl was also quantified from the total integrated OH absorbance using the mineral-specific absorption coefficient (Bell et al., 2003). The sum of all hydroxyl absorptions, calculated from different crystals from the same sample, were always identical (±<10% relative). Different hydroxyl contents are generated for each sample (Table 4) because each method of quantifying hydroxyl in olivine yields a unique concentration from identical OH absorbance intensities. Using our preferred calibration, (Libowitzky and Rossman, 1997) (see Grant et al. (2006) for a discussion), the hydroxyl contents of synthetic forsterite crystals described here range from 10 to 23 ppm H_2O (Table 4).

3.4. Hydrous species in enstatite

Polarised infrared absorbance spectra of enstatite from ALB5, ALB6, ALB7, ALB9 and ALB13 are shown on Fig. 3. No enstatite crystals suitable for infrared analysis were recovered from ALB8 and none at all were found in ALB10. Hydroxyl species in enstatite from ALB5, ALB6, ALB7, ALB13 and ALB14 (not shown on Fig. 3) are identical. Measured where E||*a*, OH modes in these samples occur at 3600 and 3390 cm^{-1}. Measured with E||*b*, a strong absorption at 3600 cm^{-1}, a double mode at 3554 and 3515 cm^{-1} and two broader bands at 3390 and 3044 cm^{-1} are identified. OH modes measured E||*c* are found at 3554, 3515, 3474, 3390 and 3061 cm^{-1}. OH vibrations in enstatite from ALB9, which at 2.5 GPa was the highest pressure experiment performed, generate somewhat broader absorptions than those of the other samples and, on spectra measured where E||*c*, have peak maxima at slightly different vibrational energies to those of the other samples. Where E||*c*, OH defects in enstatite crystals from run ALB9 generate bands at 3574, 3522, 3400 and 3306 cm^{-1}.

We attempted to resolve enstatite spectra into discrete hydroxyl absorptions using an identical method to that used for forsterite. However, although the vibrational energies of OH maxima were identical in every crystal

Table 4
OH absorbance intensities and corresponding hydroxyl contents in synthetic forsterite

Vibrational energy of OH absorption (cm^{-1})											
	3612	3593	3566	3381	3346	3322	3222	3160	Abs[1]	H_2O[2]	H_2O[3]
E||*a*											
ALB5	3	8	–	9	49	8	–	–	77	5.3	7.9
ALB6	5	–	–	8	43	20	–	–	75	4.7	7.1
ALB8	7	–	–	29	76	11	–	–	123	7.7	11.7
ALB10	7	11	4	3	49	6	–	–	81	6.0	9.5
E||*b*											
ALB5	–	–	–	7	16	5	–	–	27	1.5	2.3
ALB6	–	–	–	5	16	7	–	–	28	1.6	2.4
ALB8	–	–	–	2	18	8	–	–	28	1.6	2.5
ALB10	–	61	–	11	12	6	–	–	90	10.0	14.7
E||*c*											
ALB5	–	–	–	7	27	32	–	12	78	4.1	6.3
ALB6	–	–	–	3	23	18	–	28	72	3.5	5.4
ALB8	–	–	–	6	51	35	–	47	138	6.8	10.5
ALB10	–	–	–	7	33	21	35	33	129	6.0	9.5

Note. All integrated absorbances have been normalised to a 1 cm pathlength.
[1]Sum of integrated OH absorbances measured parallel to each crystallographic orientation for each sample. Wt ppm H_2O in forsterite was calculated using [2]Libowitzky and Rossman (1997) and [3]Paterson (1982).

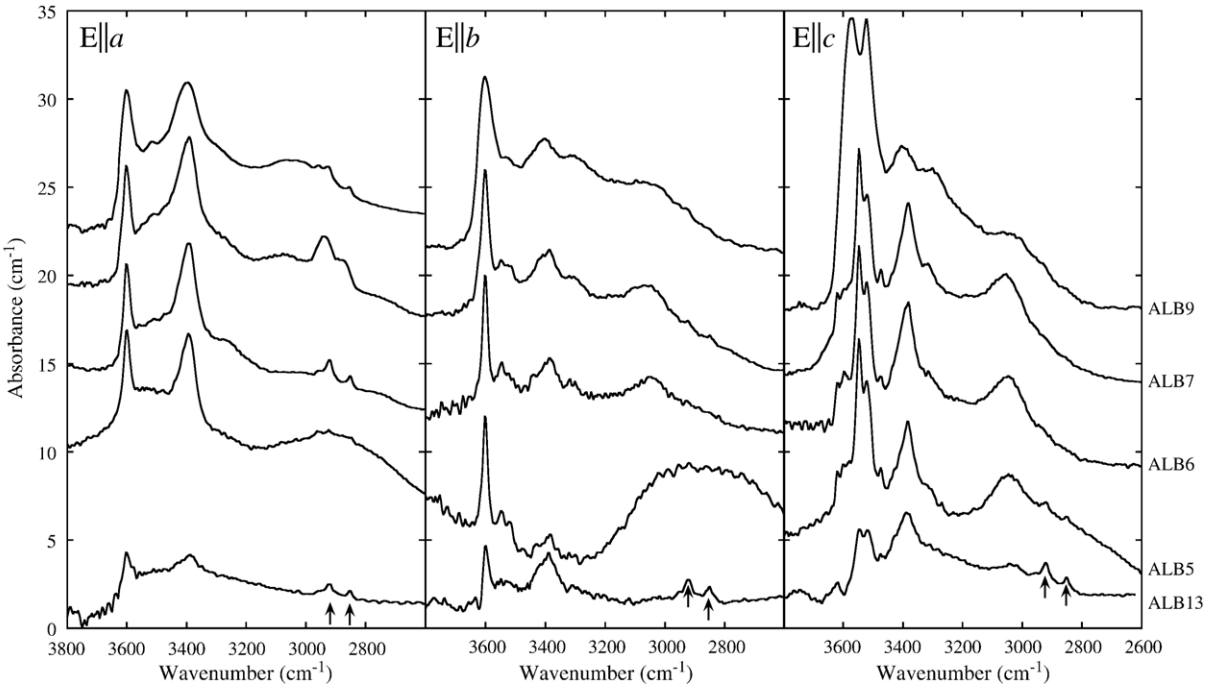

Fig. 3. Polarised absorbance spectra showing OH species in enstatite from samples ALB13, ALB5, ALB6, ALB7 and ALB9. All spectra shown on the figure are the results of single analyses where the incident beam was aligned parallel to the crystallographic axes of the crystals. The arrows indicate bands attributed to C–H vibrations from residual resin. These are not thought to be intrinsic to enstatite.

from a sample, the integrated OH absorbance (the absorbance intensity) differed greatly. Different enstatite crystals from an experiment yield highly variable total water contents. Problematically, this indicates that the amount of hydroxyl dissolved in enstatite from each sample was heterogeneous or that crystals contain homogeneous concentrations of intrinsic hydroxyl defect species but develop different absorption morphologies and therefore, intensities, because of a further, and highly variable, contribution. To better understand the origins of these spectral variabilities, and to quantify the range of total water contents that crystals from each sample contained, we analysed as many different enstatite crystals as possible from every experiment and examined the spectral data closely. We noted that if the intensity of an OH peak was crudely defined as the difference between the height of the local OH absorption maximum and that of an adjacent minimum, OH absorption intensities in every crystal from an experiment were remarkably similar (Fig. 4). Subtracting a thickness-normalised spectrum with high water contents (spectrum E on Fig. 4) from one from the same experiment, but which contains less water (spectrum A, Fig. 4), generates a broad-band residual component (Fig. 4). We also collected two perpendicularly polarised spectra through the same point in the same crystal of a sample containing apparently high water contents. When we then subtracted similarly polarised spectra containing low water contents from the two high water containing spectra, the magnitude of the residual component was identical in both. Equilibrium, intrinsic hydroxyl concentrations were quantified by fitting each of the recognisable hydroxyl absorptions on a spectrum and subtracting two broad-band absorptions at the energy and general shape of the residual ‘contaminant’ bands. Thus, the contribution of the broad component to the sample water contents was not included. Hydroxyl contents were quantified by applying the mineral-specific absorption coefficient (Bell et al., 1995) and absorption coefficients obtained through two wavenumber-dependant calibrations (Paterson, 1982; Libowitzky and Rossman, 1997) to the total integrated intrinsic OH absorbance.

Hydroxyl concentrations dissolved in enstatite differed greatly between experiments. Using our preferred calibration (Libowitzky and Rossman, 1997), enstatite from ALB5 and ALB6 contained approximately 270 ppm H_2O. Crystals from ALB7 and ALB9 contained 345 and 460 ppm H_2O, rspectively. Enstatite from ALB13, which was synthesised from starting materials containing approximately 3 wt.% H_2O contained 135 ppm H_2O. Enstatite crystals from ALB14 were extremely small and

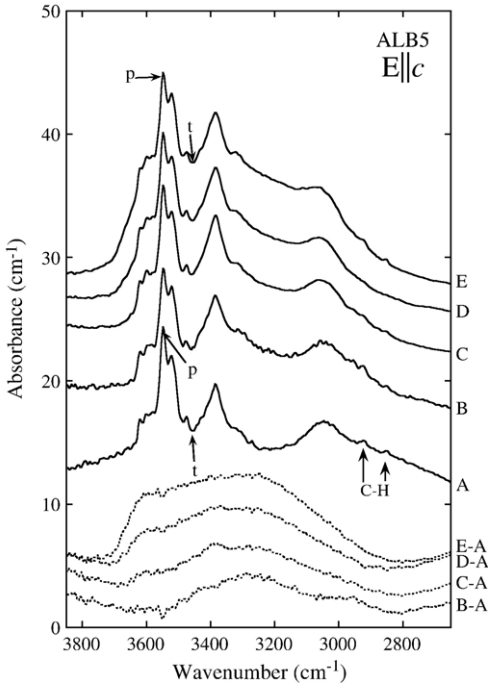

Fig. 4. Polarised spectra measured where E||*c* in five enstatite crystals from ALB5. The difference between the intensity of a peak maximum (*p*) and an adjacent trough (*t*) is essentially constant in each spectrum, however, subtracting a similar broad background to each yields five different total integrated OH absorbance intensities. Dashed lines represent the results of subtracting spectra B, C and D from spectrum A. Spectra B–A, C–A and D–A show that a highly variable broad-band component is present in most of the synthetic enstatite crystals studied. A discussion of these bands is given in the text. Arrows indicate vibrations of residual resin and are unlikely to be intrinsic to the samples.

only three polarised spectra where E||*c* and one spectrum where E||*a* were obtained. The integrated OH absorbances measured where E||*a* and E||*c* on crystals of enstatite from ALB14 were approximately 2/3 that measured on similarly oriented enstatite spectra from ALB13. Because no E||*b* spectra were collected from ALB14 the integrated OH absorbance measured parallel to this crystallographic direction for this sample was estimated to be 2/3 the intensity of the *b* component from samples ALB13 (Table 5). The total hydroxyl contents of enstatite from ALB14 were, therefore calculated as: $A^{\mathrm{tot}}=A^{\mathrm{E}\|a}+(A^{\mathrm{E}\|b\ \mathrm{ALB13}}*2/3)+A^{\mathrm{E}\|c}$.

3.5. Water in the melt

Water contents of synthetic glasses were calculated from unpolarised infrared absorbance spectra and, more crudely, through the bulk chemical analyses as determined by electron microprobe. The integrated absorbance of the band at 5200 cm^{-1} was quantified after subtracting a polynomial baseline from between approximately 5500 and 4700 cm^{-1}. The precise frequencies of the end points for the baseline depended upon the nature of the individual spectrum and differed between samples. The band centred at 4500 cm^{-1} lies on the tail of a complex sequence of bands at lower vibrational energies and so subtracting a baseline in this region proved difficult. The integrated absorbance of the 4500 cm^{-1} band was estimated by fitting a Gaussian peak to the same background-subtracted spectrum used to estimate the integrated absorbance of the 5200 cm^{-1} band. OH and H_2O concentrations were estimated from the integrated absorbance of the 5200 and 4500 cm^{-1} bands using $c=100*18.02A/\rho d\varepsilon$, where A is the integrated absorbance of the band, ρ the density, d the thickness, and ε the absorption coefficient. Melt density (ρ) was calculated for each sample individually using the function presented for albite glasses (Behrens et al., 1996). Absorption coefficients (ε) used in these calculations (241 (l mol^{-1} cm^{-1}) for the H_2O band centred at 5200 cm^{-1} and 281 (l mol^{-1} cm^{-1}) for the OH band at 4500 cm^{-1}) were published previously (Withers and Behrens, 1999).

Table 5
Thickness-normalised integrated OH absorbance intensities in aluminous enstatite

	E||*a*				E||*b*			E||*c*			Sum		
	$A^{E\|\|a}$	H_2O^1	H_2O^2	$A^{E\|\|b}$	H_2O^1	H_2O^2	$A^{E\|\|c}$	H_2O^1	H_2O^2	A^{sum}	H_2O^1	H_2O^2	H_2O^3
AlB5	625	60	44	854	92	53	1496	113	84	2975	265	181	201
ALB6	745	75	55	782	84	49	1452	109	81	2979	268	1 85	201
ALB7	951	92	67	1131	121	71	1748	132	98	3830	345	236	258
ALB9	1488	144	105	1356	146	85	2220	168	124	5064	458	314	341
ALB13	222	22	16	649	69	40	587	44	32	1 458	135	88	98
ALB14	158	15	11	433[4]	46	27	412	30	20	1003	91	58	68

Note: Absorbance intensities are intrinsic hydroxyl defect species only and have been normalised to a 1 cm pathlength. A is the total integrated OH absorbance measured with the electric vector aligned parallel to the superscripted crystallographic orientation. Dissolved hydroxyl contents were qualified using [1]Libowitzky and Rossman (1999), [2]Paterson (1982), [3]Bell et al. (1995), and [4]estimated by multiplying intensity measured where E||*b* in enstalite from ALB 13 by 2/3 (see text).

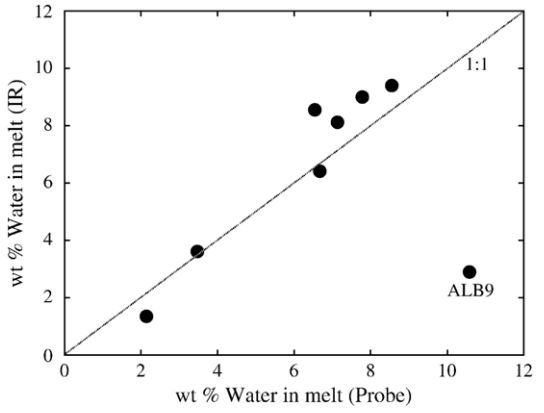

Fig. 5. Water contents of the quenched melt estimated through applying an integral absorption coefficient to the water absorptions identified on infrared spectra and by difference of oxide totals measured using the electron microprobe.

Glass water contents were also estimated using the shortfall technique on the electron microprobe. This technique is based on the assumption that electron microprobe analysis should sum to 100%. If the observed total is lower than this, the difference is attributed solely to the presence of undetectable elements such as H. In general, water contents obtained using the two techniques correlate reasonably well (Fig. 5). The average water content of the glass in ALB 9 estimated by difference from the electron microprobe analyses (10.6 wt.%) is, however, significantly greater than that estimated using the infrared spectrum (2.9 wt.%). The cause of this discrepancy remains uncertain, but water content calculated using infrared spectra is judged more reliable than the EPMA method because additional volatile elements in the sample likely contribute to the 'missing' data when using the later. The value of 2.9 wt.% H_2O obtained using the infrared spectra is therefore preferred. As a check on the validity of this assumption, relative melt water contents of ALB9 and several other samples were also estimated using the relative intensities of the fundamental water modes in the glass. This was achieved by analysing extremely thin slices of glass (approximately 10 μm). The results were consistent with concentrations derived from the 4500 cm^{-1} and 5200 cm^{-1} peaks.

Using infrared spectra, glass from ALB5, ALB6, ALB7 and ALB10 contains 8.1, 9.0, 9.4 and 8.6 wt.% H_2O respectively. Glass from ALB13 contains 3.6 wt.% H_2O whilst that from ALB14 contains approximately 1.3 wt.% H_2O (Table 6).

4. Discussion

4.1. Hydrous defect species in forsterite

Hydroxyl in pure forsterite generates a number of sharp absorptions between 3650–3400 cm^{-1} and/or two broad absorptions centred at 3230 and 3160 cm^{-1} (Lemaire et al., 2004; Berry et al., 2005; Grant et al., 2006; Smyth et al., 2006). Experiments conducted at different $aSiO_2$ suggest that absorptions between 3650–3400 cm^{-1} correspond to OH on silicon vacancies ($V_{Si''''}$) and those between 3230–3160 cm^{-1} OH at Mg vacancies ($V_{Mg''}$) (Lemaire et al., 2004; Berry et al., 2005; Grant et al., 2006). Calculated vibrational energies agree with these assignments (Braithwaite et al., 2003; Walker et al., 2006). Absorptions at 3650–3400 cm^{-1} have, however, also been attributed to OH at Mg vacancies (Smyth et al., 2006) and low-frequency vibrations (3400–3000 cm^{-1}) to OH at paired Mg vacancies (Keppler and Bolfan-Casanova, 2006). Most natural olivines, and those annealed at high water activity, generate absorptions at 3650–3500 cm^{-1}.

Table 6
Summary of water concentrations in all phases and derived partition coefficients

	P	T	H_2O En[1]	H_2O En[2]	H_2O Fo[1]	H_2O Fo[3]	H_2O Melt^{EMPA}	H_2O Melt^{IR}	$D_{H_2O}^{En/Fo}$	$D_{H_2O}^{En/melt}$	$D_{H_2O}^{Fo/melt}$
	(GPa)	(°C)	(ppm)	(ppm)	(ppm)	(ppm)	(wt.%)	(wt.%)			
ALB5	1.5	1295	265	201	11	33	7.1	8.1	24	0.003	0.0001
ALB6	1.5	1320	268	201	10	34	7.8	9.0	27	0.003	0.0001
ALB7	2.0	1305	345	258	–	–	8.6	9.4	–	0.004	–
ALB8	2.0	1339	–	–	16	54	6.7	6.4	–	–	0.0003
ALB9	2.5	1330	457	340	–	–	10.6	2.9	–	0.016	–
ALB10	1.0	1320	–	–	22	56	6.5	8.6	–	–	0.0003
ALB13	1.5	1350	135	97	–	–	3.5	3.6	–	0.004	–
ALB14	1.5	1400	91	68	–	–	2.1	1.3	–	0.007	–

Note. Hydroxyl contents (in wt ppm H_2O) were calculated using [1]Libowitzky and Rossman (1997), [2]Bell et al. (2003), [3]Bell et al. (1995). Partition coefficients were calculated using the wavenumber-dependant calibration and melt water contents measured using IR data.

These are interpreted as OH defects at M-site vacancies (Kohlstedt et al., 1996; Mosenfelder et al., 2006a,b) or hydrated Ti-related defects (Berry et al., 2005).

Forsterite from ALB5, ALB6 and ALB8 contain hydroxyl defects with vibrational energies at about 3160 cm^{-1} and a group of absorptions at 3381, 3346 and 3322 cm^{-1}. OH absorptions at 3160 are consistent with high $a SiO_2$ (Lemaire et al., 2004; Berry et al., 2005). Absorptions at 3381, 3346 and 3322 cm^{-1} are not observed in pure forsterite (Lemaire et al., 2004; Berry et al., 2005; Grant et al., 2006). "Pure" forsterite crystals containing absorptions in this energy region contain trace concentrations of impurity elements (Zhao et al., 2004). As the olivine crystals in this study are aluminium-bearing (Table 3) we assign absorptions at 3381, 3346 and 3322 cm^{-1} to Al^{3+}-related OH groups, where H charge balances a substitution such as $Al^{3+} \Leftrightarrow Si^{4+}$ or $Al^{3+} \Leftrightarrow 2Mg^{2+}$. This assignment has two important implications:

i) Olivine without OH absorptions at 3381, 3346 and 3322 cm^{-1} are unlikely to incorporate protons via a charge balanced substitution with Al. This observation could be used to test models of water solubility that postulate a relationship between Al and H in olivine (*e.g.* Hauri et al., 2006).

ii) As Fe^{3+} and Al^{3+}-related hydroxyl defects are likely to generate similar absorption characteristics, several other features commonly observed in natural olivines can be explained. Absorptions at 3355 and 3325 cm^{-1} are prominent in many synthetic olivines (Bai and Kohlstedt, 1993; Matveev et al., 2001) and have been attributed to H at M-site vacancies because they appear to be enhanced at high silica activity (Matveev et al., 2005). However, absorptions in this region are also enhanced under oxidising conditions (Bai and Kohlstedt, 1993; Mosenfelder et al., 2006a,b) and the exponent of the oxygen fugacity dependence was used to suggest that they are related to singly-charged oxygen interstitials (Bai and Kohlstedt, 1993). However, by ascribing hydroxyl absorptions at 3381, 3346 and 3322 cm^{-1} to aluminium-related hydroxyl defects, the results of this study, and those of further work where San Carlos olivine annealed under hydrous and oxidising conditions develop absorptions at 3355 and 3325 cm^{-1} and a small peak at 3306 cm^{-1} (Grant et al., submitted for publication), interpreted as the result of the analogous Fe^{3+} substitution, lead us to suggest that all hydroxyl modes between 3400–3200 cm^{-1} in olivine are associated with hydroxyl defects associated with trivalent cations in the olivine structure.

Forsterite from one experiment (ALB10) contains hydroxyl species with vibrational energies between 3650 and 3400 cm^{-1}. Spectra from ALB10 are very similar to those of forsterite from EN2, an Al_2O_3 contaminated experiment conducted in the system $MgO–SiO_2–H_2O$ (Grant et al., 2006) (Fig. 2). Why defect species with vibrational energies between 3650—3400 cm^{-1} develop in some forsterite samples and not others in this study remains unclear, although it may be related to elevated $a H_2O$ in ALB10, relative to the other samples we describe, because of similarities with water-saturated crystals from EN2. The effect of $a H_2O$ on hydroxyl defect speciation in olivine deserves further exploration.

Absorptions at similar vibrational energies to the Al^{3+}-related OH defects described here have been reported in natural, mantle-derived olivine (Matsyuk and Langer, 2004). Previous studies have shown that OH defect speciation in mantle-derived olivine is extremely complex, and upwards of 10 different OH bands with energies between 3400 and 3300 cm^{-1} have been identified (Matsyuk and Langer, 2004). Further studies into the influence of different trivalent cations on the OH stretching signature of forsterite may prove an important mechanism for identifying a diverse range of cation impurities in mantle olivine. As many trace elements are highly incompatible in olivine, the concentrations of such elements are generally below the detection limit of electron microprobe analysis. Correlating the vibrational frequencies of specific hydrous species associated with different trivalent cations could be used as a tool to trace the extent of metasomatic events as recorded in olivine from mantle xenoliths. Further controlled experiments are, however, necessary to investigate this possibility further and link trace element impurities with specific OH bands.

Hydroxyl concentrations in forsterite described here are lower than those reported in pure forsterite synthesised in the system $MgO–SiO_2–H_2O$ (Grant et al., 2006). Presumably this is largely because experiments described here were not water-saturated. However, forsterite from ALB10 contains hydroxyl concentrations similar to those from EN2 (Grant et al., 2006) suggesting that ALB10 must have been close to water saturation. Further studies are necessary to assess the relative roles of water fugacity, pressure, temperature and contamination by ppm levels of different trace elements in regulating the amount of water dissolved in olivine in the upper mantle. Such studies will require

trace element and water concentrations to be measured on the same samples. Furthermore, independent methods of determining water concentrations (*e.g.* SIMS) are also required to work around the uncertainties in FTIR calibrations for samples with different spectra (and hence different OH defects).

4.2. Hydrous defect species in enstatite

Hydroxyl species dissolved in the Al-bearing enstatite crystals described in this study are very different from those in Al-free enstatite (Mierdel and Keppler, 2004; Grant et al., 2006), but comparable with other synthetic and natural Al-bearing orthopyroxenes (Rauch and Keppler, 2002; Stalder and Skogby, 2002; Stalder, 2004; Stalder et al., 2005). Hydroxyl speciation in enstatite synthesised in the Alb–Fo–H_2O system at 1.5 GPa and 1320 °C is broadly similar to that in natural crystals from a kimberlite-hosted garnet peridotite xenolith (Grant et al., 2007). Hydroxyl species present in enstatite from water-rich experiments are identical to those from experiments conducted at lower water fugacities (ALB13, ALB14). This important observation indicates that hydroxyl speciation in aluminous enstatite is not controlled by water fugacity but is (in Fe-free systems, at least) largely controlled bulk chemical composition. Hydroxyl incorporation into aluminous enstatite *via* coupled substitution of Al^{3+} H^{+} either for Si^{4+} or $2Mg^{2+}$ has been proposed by several authors (Rauch and Keppler, 2002; Kohn et al., 2005). However, direct measurements of Al environments using ^{27}Al NMR (Kohn et al., 2005) suggest that the ratio of tetrahedral Al:octahedral Al is identical for dry and water-saturated aluminous enstatite. Thus the dominant mechanism of Al incorporation in both cases is solid solution of Mg-Tschermaks component, $MgAl_2SiO_6$. In the water-undersaturated aluminous enstatite from the present study, the change in (Mg + Si) as a function of Al (on an atomic basis) is in excellent agreement with the expectation of Mg-Tschermaks solid solution. The atomic Na and H concentrations are low compared with those of Al, so it is not possible to use the concentrations of $MgAl_2SiO_6$ and $NaAlSi_2O_6$ components to deduce the incorporation mechanisms of H in enstatite.

Absolute hydroxyl concentrations in synthetic orthopyroxenes described here are lower than those reported in some previous studies (when similar Al concentrations are compared) (Stalder, 2004). This is undoubtedly because the current experiments were not water saturated, but may also be caused by different experimental procedures and perhaps because different background subtraction methods were employed. The method of background subtraction is of great concern because heterogeneous spectra from single samples have also been frequently reported in previous studies of synthetic aluminous enstatite (Rauch and Keppler, 2002; Mierdel and Keppler, 2004; Mierdel et al., 2007). Our spectra (Fig. 4) demonstrate that the total water contents of different enstatite crystals from the same experiment can vary enormously. We suspect that much of this is related melt or fluid inclusions (possibly with sub-microscopic sizes), or water trapped at defects such as dislocations and sub-grain boundaries — species that do not represent not equilibrium point-defects within the crystal structure. Our results, therefore, indicate that caution should be exercised when equilibrium dissolved hydroxyl concentrations are quantified from spectra that appear to contain a large, broad component, such as the low temperature and low pressure orthopyroxene spectra described elsewhere (Mierdel et al., 2007).

4.3. Partitioning of hydrous species between synthetic phases

Partition coefficients, which describe the partitioning of hydroxyl between coexisting phases synthesised in the system Fo–Alb–H_2O are presented on Table 6. Hydroxyl concentrations in forsterite and enstatite were calculated using the wavenumber-dependant integrated absorption coefficient (Libowitzky and Rossman, 1997). Hydroxyl partitioning between forsterite and enstatite can be calculated from the results of two experiments and a value of $D_{H_2O}^{En/Fo} = 25.1 \pm 1.5$ ($n=2$) is derived. This contrasts with the value of $D_{H_2O}^{En/Fo} = 3$ for an Al-free system under comparable conditions of pressure and temperature. The average value of $D_{H_2O}^{En/melt}$ is 0.006 ± 0.005 ($n=6$) but the large uncertainty reflects a strong compositional dependence. The average partition coefficient between forsterite and melt ($D_{H_2O}^{Fo/melt}$) is 0.0002 ± 0.0001 ($n=4$).

In the synthetic system MgO–SiO_2–H_2O, $D_{H_2O}^{En/melt}$ at 1.0 GPa and 1420 °C is estimated to be 0.0004 (Grant et al., 2006). Forsterite and enstatite did not coexist in that sample and so partitioning data involving both phases cannot be directly obtained. However, every experiment in the MgO–SiO_2–H_2O system containing both forsterite and enstatite yielded $D_{H_2O}^{En/Fo}$ of approximately 3. Therefore, if we assume that $D_{H_2O}^{En/Fo} = 3$ in the experiment containing enstatite and glass, the partitioning of water between olivine and melt ($D_{H_2O}^{Fo/melt}$) should be approximately a third of that between enstatite and melt ($D_{H_2O}^{En/melt}$). Thus, we obtain $D_{H_2O}^{Fo/melt} = 0.0001$ for

phases synthesised at 1.0 GPa and 1420 °C in the system $MgO–SiO_2–H_2O$, which is similar to that obtained in this study for experiments at 1.5 GPa (ALB5 and ALB6), both of which yield $D_{H_2O}^{Fo/melt}$ of 0.0001. $D_{H_2O}^{Fo/melt}$ for phases in ALB 8 (which was performed at 2 GPa) is 0.0003. Sample ALB10 gives $D_{H_2O}^{Fo/melt}$ of 0.0003. Identical values of $D_{H_2O}^{Fo/melt}$ in phases synthesised in Al-free and Al-bearing systems are interesting because OH defect speciation in Al-bearing and Al-free, enstatite-buffered forsterite are very different. The implication here is that the energetics of water incorporation for the two completely different OH defects are identical. Alternatively one could speculate that the actual mechanism of water incorporation in olivine is the same at high pressure and temperature, but that two different retrograde rearrangements occur upon quenching, depending on the composition. *In situ* measurements would be required to test this possibility.

Fig. 6 shows a compilation of reported values of $D_{H_2O}^{opx/melt}$ from this study and from the literature (Dobson et al., 1995; Koga et al., 2003; Aubaud et al., 2004; Grant et al., 2006; Hauri et al., 2006; Kohn and Grant, 2006) as a function of orthopyroxene Al_2O_3 contents. It is interesting to note that a striking relationship exists between the Al_2O_3 contents of orthopyroxene and $D_{H_2O}^{opx/melt}$, however, deviation from a linear correlation might indicate that additional factors, other than bulk composition, may also influence hydroxyl incorporation in iron-bearing orthopyroxene. Despite, these outliers, $D_{H_2O}^{opx/melt}$ correlates exceptionally well with orthopyroxene Al_2O_3 contents (Fig. 6). This observation is extremely important because the amount of Al_2O_3 in natural orthopyroxene can be regarded as a crude measure of the fertility of the mantle from which they derive. Thus,

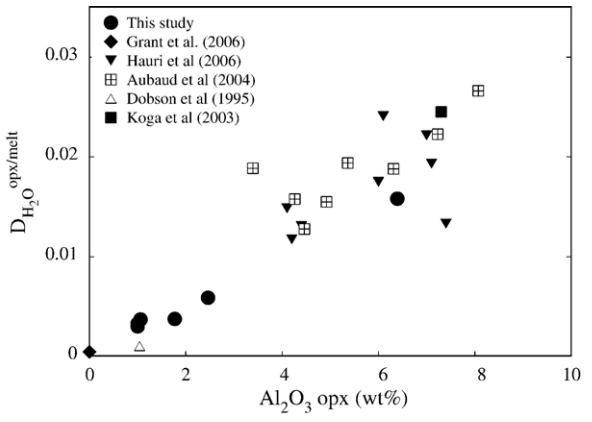

Fig. 6. Enstatite Al_2O_3 contents *versus* $D_{H_2O}^{En/melt}$ from this and a number of experimental (Koga et al., 2003; Aubaud et al., 2004; Grant et al., 2006; Hauri et al., 2006) and volcanic (Dobson et al., 1995) samples.

as mantle melting progresses along an adiabat, orthopyroxene Al_2O_3 contents will decrease, as will $D_{H_2O}^{opx/melt}$. If the same trend of changing water partition coefficient occurs for clinopyroxene, it is likely that $D_{H_2O}^{mantle/melt}$ will be a strong function of both pressure and melt fraction. These concepts have been explored by (Hauri et al., 2006), and the implications for differences in $D_{H_2O}^{mantle/melt}$ and $D_{Ce}^{mantle/melt}$ for different lithologies are discussed elsewhere (Kohn and Grant, 2006).

5. Conclusions

Al^{3+}-related hydroxyl defects dominate the hydroxyl budget of synthetic forsterite crystals synthesised in an iron-free, basalt analogue at high pressure and temperature. The vibrational characteristics of the Al^{3+}-related hydroxyl species indicate that similar absorptions in Fe-bearing systems result from Fe^{3+}-related OH species and lead us to suggest that the intensities of bands at 3300–3400 cm^{-1} in natural olivine could form the basis of an oxybarometer.

Hydroxyl speciation in aluminous enstatite is controlled by bulk chemistry and is not influenced water activity. A non-intrinsic broad-band hydrous component contributed highly variable amounts of water to the overall budget of synthetic enstatites from any single experiment. This extrinsic contribution is relatively commonplace in synthetic, aluminous enstatites and indicates that caution should be exercised when extracting dissolved water concentrations from spectra with a large broad component. Intrinsic hydroxyl concentrations dissolved in enstatite are identical in all crystals from an experiment.

The partitioning of hydroxyl species between forsterite, enstatite and coexisting silicate melt is not controlled by pressure, temperature and total water content over the range of conditions studied. The partitioning of hydroxyl between forsterite and melt is insensitive to pressure or olivine aluminium contents. In contrast, $D_{H_2O}^{En/melt}$ is strongly controlled by enstatite Al_2O_3 contents.

Acknowledgements

We are grateful to NERC for research grant NER/A/S/2002/00871. KG acknowledges additional support from an Australian Government Federation Fellowship to Prof. B. Wood. This study used instrumentation and geochemical laboratories funded by ARC LIEF and DEST Systemic Infrastructure Grants, Macquarie University and industry. Andrew Berry, Jannick Ingrin and Bernie Wood are thanked for helpful discussions, and

Roland Stalder and an anonymous reviewer for their comments. This is contribution no. 474 from the ARC GEMOC National Key Centre (www.es.mq.edu.au/GEMOC/).

References

Aubaud, C., Hauri, E.H., Hirschmann, M.M., 2004. Water partition coefficients between nominally anhydrous minerals and basaltic melts. J. Geophys. Res. 31, L20611. doi:10.1029/22004GL021341.

Bai, Q., Kohlstedt, D.L., 1993. Effects of chemical environment on the solubility and incorporation mechanism for hydrogen in olivine. Phys. Chem. Miner. 19, 460–471.

Behrens, H., Romano, C., Nowak, H.L., Holtz, F., Dingwell, D.B., 1996. Near-infrared spectroscopic determination of water species in glasses in the system $MAlSi_3O_8$ (M=Li, Na, K): an interlaboratory study. Chem. Geol. 128, 41–63.

Bell, D.R., Ihinger, P.D., Rossman, G.R., 1995. Quantitative analysis of trace OH in garnet and pyroxenes. Am. Mineral. 80, 465–474.

Bell, D.R., Rossman, G.R., Maldener, J., Endisch, D., Rauch, F., 2003. Hydroxide in olivine: a quantitative determination of the absolute amount and calibration of the IR spectrum. J. Geophys. Res. 108, 2105.

Berry, A.J., Hermann, J., O'Neill, H.S.C., Foran, G.J., 2005. Fingerprinting the water site in mantle olivine. Geology 33, 869–872.

Braithwaite, J.S., Wright, K., Catlow, C.R.A., 2003. A theoretical study of the energetics and IR frequencies of hydroxyl defects in forsterite. J. Geophys. Res. 108, 1–9.

Dobson, P.F., Skogby, H., Rossman, G.R., 1995. Water in boninite glass and coexisting orthopyroxene: concentration and partitioning. Contrib. Mineral. Petrol. 118, 414–419.

Grant, K.J., Kohn, S.C., Brooker, R.A., 2006. Solubility and partitioning of water in synthetic forsterite and enstatite in the system MgO–SiO_2–H_2O±H_2O. Contrib. Mineral. Petrol. 151, 651–664.

Grant, K.J., Ingrin, J., Lorand, J.-P., Dumas, P., 2007. Water partitioning between mantle minerals from peridotite xenoliths. Contrib. Mineral. Petrol. 154, 15–34.

Grant, K.J., Brooker, R.A., Kohn, S.C., Wood, B.J., submitted for publication. The effect of oxygen fugacity on hydroxyl concentrations and speciation in olivine: implications for water solubility in the upper mantle, Earth Planet. Sci. Lett.

Hirth, G., Kohlstedt, D.L., 1996. Water in the oceanic upper mantle: implications for rheology, melt extraction and the evolution of the lithosphere. Earth Planet. Sci. Lett. 144, 93–108.

Hirschmann, M.M., Aubaud, C., Withers, A.C., 2005. Storage capacity of H_2O in nominally anhydrous minerals in the upper mantle. Earth Planet. Sci. Lett. 236, 167–181.

Hauri, E.H., Gaetani, G.A., Green, T.H., 2006. Partitioning of H_2O between mantle minerals and silicate melts. Earth Planet. Sci. Lett. 248, 715–734.

Ingrin, J., Blanchard, M., 2006. Diffusion of hydrogen in mantle minerals. Rev. Mineral. Geochem. 62, 291–320.

Ingrin, J., Skogby, H., 2000. Hydrogen in nominally anhydrous upper-mantle minerals: concentration levels and implications. Eur. J. Mineral. 12, 543–570.

Jamtveit, B., Brooker, R.A., Brooks, K., Larsen, L.M., Pederson, T., 2001. The water content of olivines from the North Atlantic Volcanic Province. Earth Planet. Sci. Lett. 186, 401–415.

Karato, S., 1990. The role of water in the electrical conductivity of the upper mantle. Nature 347, 272–273.

Keppler, H., Bolfan-Casanova, N., 2006. Thermodynamics of water solubility and partitioning. Rev. Mineral. Geochem. 62, 193–230.

Koga, K., Hauri, E., Hirschmann, M.M., Bell, D.R., 2003. Hydrogen concentration analyses using SIMS and FTIR: comparison and calibration for nominally anhydrous minerals. Geochem. Geophys. Geosyst. 4, 1019. doi:10.1029/2002GC00378.

Kohlstedt, D.L., Keppler, H., Rubie, D.C., 1996. Solubility of water in the α-phase, β-phase and γ-phase of $(MgFe)_2SiO_4$. Contrib. Mineral. Petrol. 123, 345–357.

Kohn, S.C., Grant, K.J., 2006. The partitioning of water between nominally anhydrous minerals and silicate melts. Rev. Mineral. Geochem. 62, 231–241.

Kohn, S.C., Roome, B.M., Smith, M.E., Howes, A.P., 2005. Testing a potential mantle geohygrometer; the effect of dissolved water on the intracrystalline partitioning of Al in orthopyroxene. Earth Planet. Sci. Lett. 238, 342–350.

Lemaire, C., Kohn, S.C., Brooker, R.A., 2004. The effect of silica activity on the incorporation mechanisms of water in synthetic forsterite: a polarised infrared spectroscopic study. Contrib. Mineral. Petrol. 147, 48–57.

Libowitzky, E., Rossman, G.R., 1996. Principles of quantitative absorbance measurements in anisotropic crystals. Phys. Chem. Miner. 23, 319–327.

Libowitzky, E., Rossman, G.R., 1997. An IR absorption calibration for water in minerals. Am. Mineral. 82, 1111–1115.

McDade, P., Wood, B.J., Van Westrenen, W., Brooker, R.A., Gudmundsson, G., Soulard, H., Najorka, J., Blundy, J.D., 2002. Pressure corrections for a selection of piston-cylinder assembles. Mineral. Mag. 66, 1021–1028.

Mosenfelder, J.L., Deligne, N.I., Asimow, P.D., Rossman, G.R., 2006a. Hydrogen incorporation in olivine from 2–12 GPa. Am. Mineral. 91, 285–294.

Mosenfelder, J.L., Sharp, T.G., Asimow, P.D., Rossman, G.R., 2006b. Hydrogen incorporation in natural mantle olivines. Water in the mantle. American Geophysical Union, Washington.

Matveev, S., O'Neill, H.S.C., Ballhaus, C., Taylor, W.R., Green, D.H., 2001. Effect of silica activity on OH-IR spectra of olivine: implications for low $aSiO_2$ mantle metasomatism. J. Petrol. 42, 721–729.

Matveev, S., Portnyagin, M., Ballhaus, C., Brooker, R.A., Geiger, C.A., 2005. FTIR spectrum of phenocryst olivine as an indicator of silica saturation in magmas. J. Petrol. 46, 603–614.

Matsyuk, S.S., Langer, K., 2004. Hydroxyl in olivines from mantle xenoliths in kimberlites of the Siberian Platform. Contrib. Mineral. Petrol. 147, 413–437.

Mierdel, K., Keppler, H., 2004. The temperature dependence of water solubility in enstatite. Contrib. Mineral. Petrol. 148, 305–311.

Mierdel, K., Keppler, H., Smyth, J.R., Lagenhorst, F., 2007. Water solubility in aluminous orthopyroxene and the origin of the Earth's asthenosphere. Science 315, 364–368.

Norman, M.D., Pearson, N.J., Sharma, A., Griffin, W.L., 1996. Quantitative analysis of trace elements in geological materials by laser ablation ICPMS: instrumental operating conditions and calibration values of NIST glasses. Geostand. Newsl. 20, 247–261.

Regenauer-Lieb, K., Kohl, T., 2003. Water solubility and diffusivity in olivine: its role in planetary tectonics. Mineral. Mag. 67, 697–715.

Rauch, M., Keppler, H., 2002. Water solubility in orthopyroxene. Contrib. Mineral. Petrol. 143, 525–536.

Paterson, M.S., 1982. The determination of hydroxyl by infrared absorption in quartz, silicate glasses and similar materials. Bull. Minéral. 105, 20–29.

Stalder, R., 2004. Influence of Fe, Cr and Al on hydrogen incorporation in orthopyroxene. Eur. J. Mineral. 16, 703–711.

Stalder, R., Skogby, H., 2002. Hydrogen incorporation in enstatite. Eur. J. Mineral. 14, 1139–1144.

Stalder, R., Klemme, S., Ludwig, T., Skogby, H., 2005. Water incorporation in orthopyroxene: interaction of different trivalent cations. Contrib. Mineral. Petrol. 150, 473–485.

Smyth, J.R., Frost, D.R., Nestola, F., Holl, C.M., Bromiley, G., 2006. Olivine hydration in the deep upper mantle: effects of temperature and silica activity. Geophys. Res. Lett. 33. doi:10.1029/2006GL026194.

Walker, A.M., Demouchy, S., Wright, K., 2006. Computer modelling of the energies and vibrational properties of hydroxyl groups in alpha- and beta-Mg_2SiO_4. Eur. J. Mineral. 18, 529–543.

Wang, D., Mookherjee, M., Xu, Y., Karato, S., 2006. The effect of water on the electrical conductivity of olivine. Nature 433, 977–980.

Withers, A.C., Behrens, H., 1999. Temperature induced changes in the NIR spectra of hydrous albitic and rhyolitic glasses between 100 and 300 K. Phys. Chem. Miner. 27, 119–132.

Wood, B.J., 1995. The effect of H_2O on the 410-kilometer seismic discontinuity. Science 268, 74–76.

Yoshino, T., Matsuzaki, T., Yamashita, S., Katsura, T., 2006. Hydrous olivine unable to account for conductivity anomaly at the top of the asthenosphere. Nature 443, 973–976.

Zhao, Y.-H., Ginsberg, S.B., Kohlstedt, D.L., 2004. Solubility of hydrogen in olivine: dependence on temperature and iron content. Contrib. Mineral. Petrol. 23, 1–10.